

to their cave sites and that starch granules got attached to and preserved on stone tools. I cannot prove that starch from all stone tools represents direct tool function (12, 13). Core tools and scrapers were exposed to starches more often than other tool types. Three-quarters of the starch assemblage comes from chipped stone, not ground or polished tools. African Middle Stone Age lithic repertoires do not yield large quantities of dedicated grinders that would demonstrate the processing of seeds. These early grinders are simply modified cobbles and core tools (Fig. 3) (14), with a suspected use that conforms to the technological action known as “diffuse resting percussion” and “pounding” (15), which allow the grinding of plant materials. It is not clear why the tools should be mostly coated with grass starches and not so much with other types of starch. It is possible that high-starch-bearing grass refuse built up

considerably in the cave’s main chamber at times of human occupation, thus coating both tools that were used in the processing of grass seeds and others that were not. These data imply that early *Homo sapiens* from southern Africa consumed not just underground plant staples (16) but above-ground resources too.

References and Notes

1. S. Lächelt, *The Geology and Mineral Resources of Mozambique* (Direção Nacional de Geologia, Maputo, Mozambique, 2004).
2. J. Mercader, Y. Asmerom, T. Bennett, M. Raja, A. Skinner, *J. Hum. Evol.* **57**, 63 (2009).
3. J. Mercader, T. Bennett, M. Raja, *Quat. Res.* **70**, 283 (2008).
4. J. M. J. de Wet, J. R. Harlan, E. G. Price, in *Origins of African Plant Domestication*, J. R. Harlan, J. M. J. De Wet, A. B. Stemler, Eds. (Mouton, Paris, 1976), pp. 453–478.
5. J. M. J. de Wet, *Am. J. Bot.* **65**, 477 (1978).
6. National Research Council, *Lost Crops of Africa. Volume 1: Grains* (National Academy Press, Washington DC, 1996).

7. G. B. Cagampang, A. W. Kirleis, *Starch* **37**, 253 (1985).
8. K. G. Duodu et al., *J. Cereal Sci.* **35**, 161 (2002).
9. A. Caransa, W. G. M. Bakker, *Starch* **39**, 381 (1987).
10. L. H. Harbers, *J. Anim. Sci.* **41**, 1496 (1975).
11. M. Suijka, J. Jamroz, *Int. Agrophys.* **21**, 107 (2007).
12. L. Wadley, M. Lombard, *J. Archaeol. Sci.* **34**, 1001 (2007).
13. M. Lombard, *J. Hum. Evol.* **53**, 406 (2007).
14. P. Van Peer et al., *J. Hum. Evol.* **45**, 187 (2003).
15. S. A. de Beaune, *Curr. Anthropol.* **45**, 139 (2004).
16. H. Deacon, *S. Af. Archaeol. Bull.* **48**, 86 (1993).
17. This work was supported by the Canada Research Chairs program, Canada Foundation for Innovation, Social Sciences and Humanities Research Council of Canada (file no. 10-2007-0697; CID:148244), Faculty of Social Sciences/Department of Archeology at the University of Calgary, and the National Geographic Society.

Supporting Online Material

www.sciencemag.org/cgi/content/full/326/5960/1680/DC1
Materials and Methods
Tables S1 and S2
References

18 September 2009; accepted 20 October 2009
10.1126/science.1173966

Universality in Three- and Four-Body Bound States of Ultracold Atoms

Scott E. Pollack,* Daniel Dries, Randall G. Hulet

Under certain circumstances, three or more interacting particles may form bound states. Although the general few-body problem is not analytically solvable, the so-called Efimov trimers appear for a system of three particles with resonant two-body interactions. The binding energies of these trimers are predicted to be universally connected to each other, independent of the microscopic details of the interaction. By exploiting a Feshbach resonance to widely tune the interactions between trapped ultracold lithium atoms, we find evidence for two universally connected Efimov trimers and their associated four-body bound states. A total of 11 precisely determined three- and four-body features are found in the inelastic-loss spectrum. Their relative locations on either side of the resonance agree well with universal theory, whereas a systematic deviation from universality is found when comparing features across the resonance.

One of the most notable few-body phenomena is the universally connected series of three-body bound states first predicted by Efimov (1) in 1970. Efimov showed that three particles can bind in the presence of resonant two-body interactions, even in circumstances where any two of the particles are unable to bind. When the two-body scattering length a is much larger than the range of the interaction potential r_0 , the three-body physics becomes independent of the details of the short-range interaction. Surprisingly, if one three-body bound state exists, then another can be found by increasing a by a universal scaling factor, and so on, resulting in an infinite number of trimer states (2). Universality is expected to persist with the addition of a fourth particle (3–7), with two four-body states associated with each trimer (5, 7). Intimately tied to the three-body state, these tetramers do not require any additional parameters to describe their properties.

Department of Physics and Astronomy and Rice Quantum Institute, Rice University, Houston, TX 77005, USA.

*To whom correspondence should be addressed. E-mail: scott.pollack@rice.edu

Ultracold atoms are ideal systems for exploring these weakly bound few-body states because of their inherent sensitivity to low-energy phenomena, as well as the ability afforded by Feshbach resonances to continuously tune the interatomic interactions. Pioneering experiments with trapped, ultracold atoms have obtained signatures of individual Efimov states (8–12)—as well as two successive Efimov states (13, 14)—via their effect on inelastic collisions that lead to trap loss. Evidence of tetramer states associated with the trimers has also been found (13, 15). Although the locations of successive features are consistent with the predicted universal scaling, systematic deviations as large as 60% were observed and attributed to nonuniversal short-range physics (13). In the work presented here, we use a Feshbach resonance in ^7Li for which a/r_0 can be tuned over a range spanning three decades (16). This enables the observation of multiple features that are compared to universal theory.

We confine ^7Li in the $|F = 1, m_F = 1\rangle$ (where F is the total spin quantum number and m_F is its projection) hyperfine state in an elongated, cylin-

drically symmetric, hybrid magnetic—plus—optical dipole trap, as described previously (16). A set of Helmholtz coils provides an axially oriented magnetic bias field that we used to tune the two-body scattering length a via a Feshbach resonance located near 737 G (17). For $a > 0$, efficient evaporative cooling is achieved by setting the bias field to 717 G, where $a \sim 200a_0$ (a_0 is the Bohr radius), and reducing the optical-trap intensity. Depending on the final trap depth, we create either an ultracold thermal gas just above the condensation temperature T_C or a Bose-Einstein condensate (BEC) with $>90\%$ condensate fraction. For investigations with $a < 0$, we first set the field to 762 G where $a \sim -200a_0$ and proceed with optical-trap evaporation, which is stopped at a temperature T slightly above T_C . In both cases the field is then adiabatically ramped to a final value and held for a variable hold time. The fraction of atoms remaining at each time is measured via in situ polarization phase-contrast imaging (18) for clouds where the density is high, or absorption imaging in the case of lower densities.

Analyzing the time evolution of the number of atoms in the trap determines the three-body loss coefficient L_3 (8, 13, 19), as well as the four-body loss coefficient L_4 (15). Recombination into a dimer is a three-body process because a third atom is needed to conserve both momentum and energy. For $a > 0$, the dimer can be weakly bound with binding energy $\epsilon = \hbar^2/(m a^2)$ (where m is the atomic mass and \hbar is Planck’s constant h divided by 2π), whereas for $a < 0$ there are only deeply bound molecular dimers. The recombination energy released in the collision is sufficient to eject all three atoms from the trap for $a < 0$, as well as for $a > 0$ when $\epsilon \geq U$ (where U is the trap depth). In the case of the BEC data, this latter condition holds for $a \lesssim 5000a_0$. Nonetheless, we assume that all three atoms are lost for any recombination event because, even for a larger than $5000a_0$, we observe rapid three-body

loss. We ascribe this observation to a high probability for dimers to undergo vibrational relaxation collisions that result in kinetic energies much greater than U . Four-body processes proceed in a similar fashion (6, 15).

The equation describing the dynamics of three- and four-body loss is

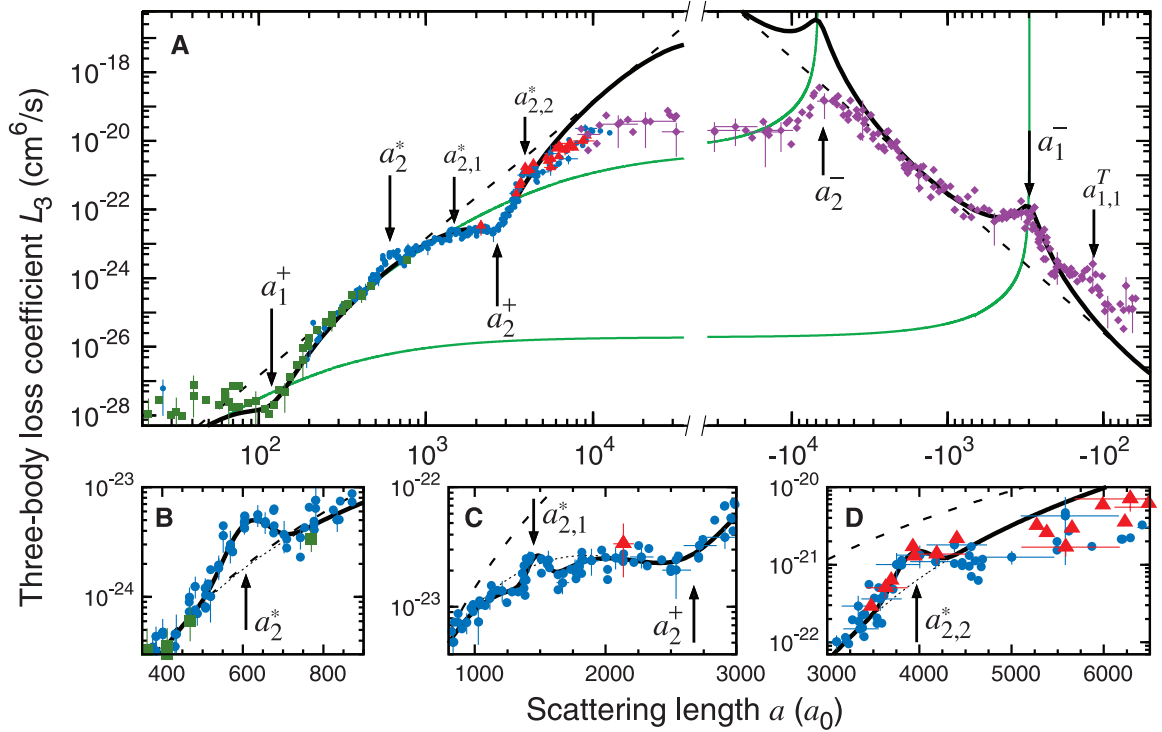
$$\frac{1}{N} \frac{dN}{dt} = -\frac{g^{(3)}}{3!} L_3 \langle n^2 \rangle - \frac{g^{(4)}}{4!} L_4 \langle n^3 \rangle \quad (1)$$

where N is the total number of atoms in the trap at time t , and the brackets denote averages over the density distribution n (17). For a thermal gas, the spatial correlation coefficients $g^{(3)}$ and $g^{(4)}$ are, respectively, $3!$ and $4!$, whereas for a BEC, both are set to 1 (20, 21). We have verified that heating from recombination is small for our short observation times and therefore omit this effect in our analysis (15, 19). By fitting the time evolution of the number of atoms to the solution of Eq. 1, we extract L_3 and L_4 as a

function of a . Figure S1 shows the loss of atoms as a function of time in regimes where either L_3 or L_4 dominates (17). Four-body loss is readily distinguished from three-body loss by the shape of the loss curve.

Figure 1 shows the extracted values of L_3 across the Feshbach resonance, exhibiting the expected a^4 scaling (22, 23), but with several dips and peaks punctuating this trend. Two prominent peaks, labeled a_1^- and a_2^- in Fig. 1A, dominate the landscape for $a < 0$. We attribute

Fig. 1. (A) L_3 as a function of a . Data shown with purple diamonds correspond to a thermal gas with $N \sim 10^6$, $T \sim 1$ to $3 \mu\text{K}$ (31), and $U \sim 6 \mu\text{K}$ and were taken with radial and axial trapping frequencies $\omega_r = (2\pi) 820 \text{ Hz}$ and $\omega_z = (2\pi) 7.3 \text{ Hz}$, respectively. The remaining data correspond to a BEC with $N \sim 4 \times 10^5$, $T < 0.5 T_G$, $U \sim 0.5 \mu\text{K}$, and $\omega_r = (2\pi) 236 \text{ Hz}$. We adjust ω_z (17) to enhance or reduce three-body loss, where $\omega_z = (2\pi) 1.6 \text{ Hz}$ (red triangles), $\omega_z = (2\pi) 4.6 \text{ Hz}$ (blue circles), and $\omega_z = (2\pi) 16 \text{ Hz}$ (green squares). The black dashed lines show an a^4 scaling, and the thick black solid lines are fits to an analytic theory (2, 17). The thin green lines show the square of the energies (in arbitrary units) of the first and second Efimov states, as predicted from the universal theory (2), where we have fixed the location of the first Efimov state to overlap with a_1^- , and the atom-dimer continuum is coincident with the dashed line for $a > 0$. Several representative error bars indicating the SE



from the fit are shown (17). **(B to D)** Detail around the loss features associated with the atom-dimer and two possible dimer-dimer resonances. The black dotted lines are fits to eq. S4, whereas the black solid lines include additional superimposed Gaussian fits to account for the features not described by eq. S4.

Table 1. Locations (in a_0) of three- and four-body loss features and inelasticity parameters (dimensionless) (17). The features $a_{2,1}^*$ and $a_{2,2}^*$ are tentatively assigned. The first number in parentheses characterizes the range over which χ^2 of the fit to theory increases by one while simultaneously adjusting the other parameters in the fit. The second number characterizes the systematic uncertainties in the determination of a (17).

$a > 0$	$a < 0$
$a_1^+ = 119(11)(0)$	$a_1^- = -298(10)(1)$
$a_2^+ = 2676(67)(128)$	$a_2^- = -6301(264)(740)$
$a_2^* = 608(11)(7)$	$a_{1,1}^T \sim -120(20)(0)$
$[a_{2,1}^* \approx 1470(15)(38)]$	$a_{1,2}^T \approx -295(35)(1)$
$[a_{2,2}^* \approx 3910(60)(278)]$	$a_{2,1}^T \approx -2950(200)(150)$
$\eta_1^+ = 0.079(32)(20)$	$a_{2,2}^T \approx -6150(800)(700)$
$\eta_2^+ = 0.039(4)(10)$	$\eta^- = 0.13(1)(3)$

Table 2. Relative locations of loss features, those predicted by theory, and the percent difference $\Delta = (\text{data/theory} - 1)$. The uncertainties are those propagated from Table 1.

	Ratio	Data	Theory	$\Delta(\%)$
$a > 0$	a_2^+/a_1^+	22.5(22)(11)	22.7*	-1(9)(5)
	a_2^+/a_2^*	4.40(14)(16)	4.46*	-1(3)(4)
	$a_{2,1}^*/a_2^*$	$\approx 2.42(5)(4)$	2.37†	+2(2)(2)
	$a_{2,2}^*/a_2^*$	$\approx 6.4(2)(4)$	6.6‡	-3(2)(6)
$a < 0$	a_2^-/a_1^-	21.1(11)(24)	22.7*	-7(5)(11)
	$a_{1,1}^T/a_1^-$	$\sim 0.40(7)(0)$	0.43†	-6(16)(0)
	$a_{1,2}^T/a_1^-$	$\approx 0.99(12)(0)$	0.90†	+10(14)(0)
	$a_{2,1}^T/a_2^-$	$\approx 0.47(4)(4)$	0.43†	+9(9)(9)
	$a_{2,2}^T/a_2^-$	$\approx 0.98(13)(1)$	0.90†	+8(14)(1)
$a \rightarrow \pm\infty$	$ a_1^- /a_1^+$	2.5(2)(0)	4.9*	-49(5)(0)
	$ a_2^- /a_2^+$	2.4(1)(4)	4.9*	-52(2)(9)
	$ a_1^- /a_2^*$	0.49(2)(1)	0.97*	-49(2)(1)
	$ a_2^- /a_2^*$	10.4(5)(14)	22.0*	-53(2)(6)

*See (2).

†See (7).

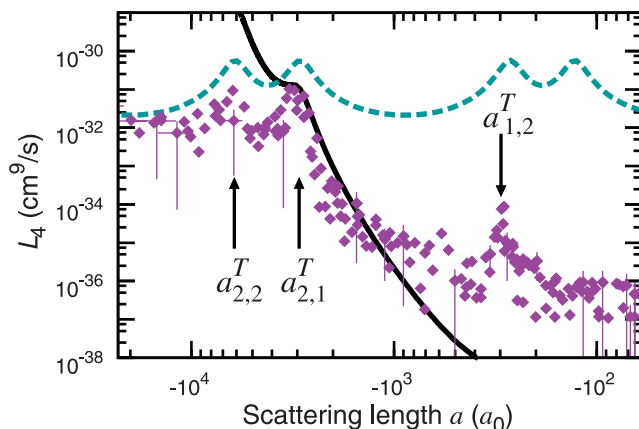
‡See (28).

these peaks to the crossings of the energies of the first two trimer states with the free-atom threshold, thus providing additional pathways into deeply bound molecular states (23). For $a > 0$, the dominant features are dips, indicated in Fig. 1A as a_1^+ and a_2^+ , corresponding to recombination minima. These minima are associated with the merging of the same two trimer states into the atom-dimer continuum and have been attributed to destructive interference between two different decay pathways into weakly bound dimers (22, 23). We fit the data to $L_3(a) = 3C(a)\hbar a^4/m$, where $C(a)$ is a logarithmically periodic function characterizing effects from the Efimov states (17). The analytic expression for $C(a)$ contains the location of one universal trimer resonance $a^- < 0$ or recombination minimum $a^+ > 0$ and an inelasticity parameter η related to the lifetime of the Efimov state (2). The observed features are fit individually to extract these parameters (Table 1). The universal theory describing Efimov physics (2) predicts a logarithmic spacing in the two-body scattering length between trimer states of $e^{\pi/s_0} \approx 22.7$, where $s_0 = 1.00624$ is a universal parameter (1). Table 2 shows that the ratios a_2^+/a_1^+ and a_2^-/a_1^- agree well with the universal theory.

A local maximum in L_3 , indicated as a_2^* and shown in detail in Fig. 1B, can be discerned between the two recombination minima a_1^+ and a_2^+ . We associate this feature with an atom-dimer resonance, given its location with respect to the nearby minima. A simple model (13) has been proposed to explain the enhanced losses present at the atom-dimer resonance. This model describes an avalanche process whereby a single dimer traveling through a collisionally thick gas shares its kinetic energy with multiple atoms, thereby increasing from three the effective number of atoms lost for each dimer formed (24).

For $a < 0$, L_3 achieves its maximum value of $\sim 10^{-19}$ cm⁶/s at a_2^- . This value is reasonably consistent with the expected unitarity limit (19, 25). At even larger values of $|a|$, L_3 saturates to a value below the unitarity limit, a behavior previously seen in experiments (8) and numerical calculations (25, 26).

Fig. 2. L_4 extracted from a thermal gas. The black solid curve is motivated by theory (17, 27), and the blue dashed curve is the solid curve divided by a^7 (6). The uncertainty in L_4 from the fit is a factor of 2, whereas the systematic uncertainty is a factor of 3 due to uncertainties in ω_r , ω_z , N , and T . For $|a| > 2 \times 10^4 a_0$, differentiation between three- and four-body losses becomes unreliable because of the very fast decay rates. Data with $L_4 < 10^{-36}$ cm⁹/s are consistent with no four-body loss.



The four-body loss coefficient (L_4) for $a < 0$ was also extracted from the data, and the results are presented in Fig. 2. Three resonant peaks in L_4 are observed, which we associate with the crossings of tetramer states with the free-atom continuum (3–7, 13, 15, 27). Two universal tetramers are predicted to accompany each Efimov trimer (5, 7). The black solid line in Fig. 2 is calculated using only the observed three-body locations and widths, in addition to an overall scaling, without any other free parameters (17). The agreement between this curve and the data lead us to assign the peaks to the second tetramer of the first Efimov trimer, $a_{1,2}^T$, and both tetramers of the second Efimov trimer, $a_{2,1}^T$ and $a_{2,2}^T$ (15). Although we do not have the resolution to detect an enhancement in L_4 at the expected location of the first tetramer $a_{1,1}^T$, an enhancement of L_3 is observed at the expected location (Fig. 1A), which we tentatively identify with $a_{1,1}^T$ (7, 13). The existence of two tetramer states tied to a single trimer state has also been verified in ¹³³Cs (15) and ³⁹K (13).

Two additional peaks in L_3 are observed on the $a > 0$ side of the resonance (Fig. 1, C and D). Features at these relative positions have not been previously observed or predicted, although they occur very close to where the two tetramer states associated with the second trimer are expected to merge with the dimer-dimer continuum (28). We have no explanation of how a dimer-dimer resonance would affect the inelastic-loss rate, as we expect the dimer fraction to be small and, consequently, the probability of dimer-dimer collisions to be negligible. One possibility is that they arise because of an interference effect, similar to that occurring in the three-body process at a_1^+ and a_2^+ . Presently, we tentatively associate these features with dimer-dimer resonances located at $a_{2,1}^*$ and $a_{2,2}^*$.

In Table 2, we present the relative spacings of observed loss features along with those predicted by the universal theory. Universal scaling is expected when $|a| \gg r_0$, where r_0 is the van der Waals radius ($33a_0$ for Li) (29). Another requirement for universality is that $|a| \gg |R_e|$, where R_e is the effective range (14). Figure S4 shows that R_e is

relatively small over the relevant field range and is $\sim -10a_0$ on resonance (17). For comparison, in the $|1, 0\rangle$ state of ⁷Li, $R_e \sim -30a_0$ at the resonance near 894 G (14). Both conditions for universality are well-satisfied for the second Efimov state, but the requirement that $|a| \gg r_0$ is only marginally satisfied for the first. Nonetheless, we find good agreement with the universal scaling relations between features on each side of the Feshbach resonance separately.

The features across a Feshbach resonance are also thought to be universally connected (2, 26). However, when we compare features across the Feshbach resonance, we find a systematic discrepancy with theory of a factor of 2 (Table 2). This discrepancy can be expressed as a difference in the three-body short-range phase between the two sides of the Feshbach resonance $\Delta\Phi = s_0 \ln(|a^-/a^+|)$ (22, 26). The locations of the features reported here result in phase differences of 0.92(10)(0) and 0.86(4)(17) (the uncertainties are defined in Table 1) for the first and second trimer, respectively, whereas the universal prediction is 1.61(3) (2). Finite temperature causes the trimer resonances to broaden and shift toward smaller $|a|$ (8, 25, 26). This would decrease the values of $\Delta\Phi$, because we extract L_3 from a thermal cloud at a^- and a much colder BEC at a^+ . Measurements of ³⁹K also show a discrepancy with theory across the resonance, but with $\Delta\Phi = 1.91(7)$ (13). On the other hand, measurements of the first trimer resonance and second trimer recombination minimum in the $|1, 0\rangle$ state of ⁷Li result in $\Delta\Phi = 1.7(2)$, in good agreement with universal theory, assuming the universal scaling of 22.7 between trimer states (14). These variations in $\Delta\Phi$ may indicate the need for additional physics to be included in the universal model (26, 30).

References and Notes

- V. Efimov, *Sov. J. Nucl. Phys. (Engl. transl.)* **12**, 589 (1971) [translation from *Yad. Fiz.* **12**, 1080 (1970)].
- E. Braaten, H.-W. Hammer, *Phys. Rep.* **428**, 259 (2006).
- L. Platter, H.-W. Hammer, U.-G. Meißner, *Phys. Rev. A* **70**, 052101 (2004).
- G. J. Hanna, D. Blume, *Phys. Rev. A* **74**, 063604 (2006).
- H.-W. Hammer, L. Platter, *Eur. Phys. J. A* **32**, 113 (2007).
- Y. Wang, B. D. Esry, *Phys. Rev. Lett.* **102**, 133201 (2009).
- J. von Stecher, J. P. D'Incao, C. H. Greene, *Nat. Phys.* **5**, 417 (2009).
- T. Kraemer *et al.*, *Nature* **440**, 315 (2006).
- S. Knoop *et al.*, *Nat. Phys.* **5**, 227 (2009).
- T. B. Ottenstein, T. Lompe, M. Kohnen, A. N. Wenz, S. Jochim, *Phys. Rev. Lett.* **101**, 203202 (2008).
- J. H. Huckans, J. R. Williams, E. L. Hazlett, R. W. Stites, K. M. O'Hara, *Phys. Rev. Lett.* **102**, 165302 (2009).
- G. Barontini *et al.*, *Phys. Rev. Lett.* **103**, 043201 (2009).
- M. Zaccanti *et al.*, *Nat. Phys.* **5**, 586 (2009).
- N. Gross, Z. Shotan, S. Kokkelmans, L. Khaykovich, *Phys. Rev. Lett.* **103**, 163202 (2009).
- F. Ferlaino *et al.*, *Phys. Rev. Lett.* **102**, 140401 (2009).
- S. E. Pollack *et al.*, *Phys. Rev. Lett.* **102**, 090402 (2009).
- Materials and methods are available as supporting material on Science Online.
- C. C. Bradley, C. A. Sackett, R. G. Hulet, *Phys. Rev. Lett.* **78**, 985 (1997).
- T. Weber, J. Herbig, M. Mark, H.-C. Nägerl, R. Grimm, *Phys. Rev. Lett.* **91**, 123201 (2003).
- Y. Kagan, B. V. Svistunov, G. V. Shlyapnikov, *JETP Lett.* **42**, 209 (1985).

21. E. A. Burt *et al.*, *Phys. Rev. Lett.* **79**, 337 (1997).
 22. E. Nielsen, J. H. Macek, *Phys. Rev. Lett.* **83**, 1566 (1999).
 23. B. D. Esry, C. H. Greene, J. P. Burke, *Phys. Rev. Lett.* **83**, 1751 (1999).
 24. J. Schuster *et al.*, *Phys. Rev. Lett.* **87**, 170404 (2001).
 25. J. P. D'Incao, H. Suno, B. D. Esry, *Phys. Rev. Lett.* **93**, 123201 (2004).
 26. J. P. D'Incao, C. H. Greene, B. D. Esry, *J. Phys. B* **42**, 044016 (2009).
 27. N. P. Mehta, S. T. Rittenhouse, J. P. D'Incao, J. von Stecher, C. H. Greene, *Phys. Rev. Lett.* **103**, 153201 (2009).
 28. J. P. D'Incao, J. von Stecher, C. H. Greene, *Phys. Rev. Lett.* **103**, 033004 (2009).
 29. T. Köhler, K. Góral, P. S. Julienne, *Rev. Mod. Phys.* **78**, 1311 (2006).
 30. P. Massignan, H. T. C. Stof, *Phys. Rev. A* **78**, 030701 (2008).
 31. In ramping from $-200a_0$ to $a < -3000a_0$, we observe an increase in the axial size of the thermal cloud that is consistent with a temperature increase of the cloud to $\sim 3 \mu\text{K}$. During the trap-loss measurements, we observe negligible change in the Gaussian width of the thermal cloud (17).
 32. We thank E. Olson for his contributions to this project and acknowledge useful discussions with E. Braaten, J. P. D'Incao, C. H. Greene, N. P. Mehta, and H. T. C. Stof. Support for this work was provided by the

NSF, Office of Naval Research, the Keck Foundation, and the Welch Foundation (grant C-1133).

Supporting Online Material

www.sciencemag.org/cgi/content/full/1182840/DC1

Materials and Methods

Figs. S1 to S4

References

5 October 2009; accepted 5 November 2009

Published online 19 November 2009;

10.1126/science.1182840

Include this information when citing this paper.

Experimental Observations of Stress-Driven Grain Boundary Migration

T. J. Rupert,^{1,2} D. S. Gianola,^{1,3} Y. Gan,⁴ K. J. Hemker^{1*}

In crystalline materials, plastic deformation occurs by the motion of dislocations, and the regions between individual crystallites, called grain boundaries, act as obstacles to dislocation motion. Grain boundaries are widely envisaged to be mechanically static structures, but this report outlines an experimental investigation of stress-driven grain boundary migration manifested as grain growth in nanocrystalline aluminum thin films. Specimens fabricated with specially designed stress and strain concentrators are used to uncover the relative importance of these parameters on grain growth. In contrast to traditional descriptions of grain boundaries as stationary obstacles to dislocation-based plasticity, the results of this study indicate that shear stresses drive grain boundaries to move in a manner consistent with recent molecular dynamics simulations and theoretical predictions of coupled grain boundary migration.

The strength and ductility of materials are inherently related to processes that govern the way that atoms move past one another, and, in crystalline metals, plastic deformation is most often associated with the way that dislocations (linear crystalline defects) move through individual crystals called grains. The mechanical behavior of metals and alloys can be tailored by introducing microstructural obstacles to dislocation motion; solid solution strengthening, precipitation hardening, and grain boundary strengthening are all examples of this. The latter is related to the fact that dislocation glide in polycrystalline metals is limited by the presence of grain boundaries and the misorientation between grains that they embody. The general realization that smaller grain-sized materials (possessing a higher density of grain boundaries) are stronger has led to the often-cited Hall-Petch relation, which states that strength scales with the reciprocal square root of grain size (1, 2) and assumes that grain boundaries act as obstacles to plastic deformation within the material.

Materials scientists traditionally describe the detailed geometric structure of grain boundaries through a coincident site lattice (CSL), which promotes the view of grain boundaries as mechanically static, immovable structures. However, recent studies involving nanocrystalline materials have introduced convincing evidence to suggest that grain boundaries are not static; mechanically induced room temperature grain growth has been associated with indentation (3–5), compression (6, 7), and tensile loading (8–11). These observations cannot be described by classical models of grain growth (8) and were originally characterized as strain-driven grain boundary migration (4). Subsequent experiments quantifying grain growth in terms of temperature (5), strain rate (10), proximity to crack tips (12), and testing mode (7) suggested that grain boundary migration in nanocrystalline metals may be driven more by stress than by plastic strain. The experiments outlined below demonstrate that the room-temperature grain growth observed in nanocrystalline metals is associated with shear stress-driven grain boundary migration, thereby confirming recent theories of coupled grain boundary migration (13, 14) and confirming that grain boundaries are not static structures as traditionally assumed.

It is widely acknowledged that shear stresses drive dislocation motion. The motion of low-angle grain boundaries, which consist of dislocation arrays, under shear stress can be described by the collective movement of the individual dislocations in these boundaries (15, 16). By

contrast, the concept of shear stress moving a high-angle grain boundary is relatively foreign to the materials science community, with experimental observations of such a mechanism being elusive. Cahn and co-workers (13) have recently published a unified theory of coupled grain boundary motion based on the supposition that the normal motion of a grain boundary couples to the tangential displacement (shear) of adjacent grains. Molecular dynamics simulations (14, 17) and bicrystal experiments (18–20) involving the migration of specific high-angle tilt boundaries have been shown to be consistent with Cahn's theory of coupled boundary migration. Recent molecular dynamics simulations (21) suggest that a fraction of general grain boundaries do exhibit anomalously high mobility when operating in a shear coupled mode, but experimental extensions to a more general population of boundaries, where grain boundaries are composed of a combination of twist and tilt character and bounded by grain boundary junctions, have proven much harder to realize. Moreover, the need for measurable grain boundary mobility requires that the bicrystal experiments be done at elevated temperature, making the separation of mechanical and thermal effects problematic. The occurrence of room-temperature grain growth in nanocrystalline metals offers the opportunity to impose much higher stresses on a much wider range of boundaries without the superposition of elevated temperature. This study was specifically designed to test the hypothesis that shear stresses can directly cause high-angle grain boundaries to move. The experiments described here allowed the investigation of the influence of normal and shear stresses and strains on the motion of a wide population of grain boundaries as encountered in most polycrystalline materials, without the need to characterize adjacent nanocrystalline grains and boundaries with high fidelity.

In order to elucidate the effect of stress and strain on mechanically induced grain growth, we have borrowed a page from the fracture mechanics community, where geometric concentrators have been used to discriminate between stress-controlled brittle fracture and strain-controlled ductile fracture (22, 23). We present experiments on freestanding nanocrystalline Al thin films, where spatial variations in the stress and strain states were deliberately introduced by using special sample geometries. A major benefit of our approach lies in

¹Department of Mechanical Engineering, Johns Hopkins University, Baltimore, MD 21218, USA. ²Department of Materials Science and Engineering, Massachusetts Institute of Technology, Cambridge, MA 02139, USA. ³Department of Materials Science and Engineering, University of Pennsylvania, Philadelphia, PA 19104, USA. ⁴Institute for Materials Research II, Karlsruhe Institute of Technology, 76131 Karlsruhe, Germany.

*To whom correspondence should be addressed. E-mail: hemker@jhu.edu